Supplementary Information

High-Precision Laser Slicing of Silicon Carbide Using Temporally Shaped Ultrafast Pulses

Yihao Yan[1], Lan Jiang[1,2,3], Zhi Wang[1], Weiyu Zhu[1], Xiaolin Qi[1], Andong Wang[1,*], David Grojo[4], Xiaowei Li[1,*]

[1] *Laser Micro/Nano Fabrication Laboratory, School of Mechanical Engineering, Beijing Institute of Technology, Beijing 100081, China*
[2] *Beijing Institute of Technology Chongqing Innovation Center, Chongqing 401120, China*
[3] *Yangtze Delta Region Academy of Beijing Institute of Technology, Jiaxing 314019, China*
[4] *Aix-Marseille University, CNRS, LP3, UMR7341, Marseille 13009, France*
Email: andong.wang@bit.edu.cn; lixiaowei@bit.edu.cn

1. Correction of spherical aberration

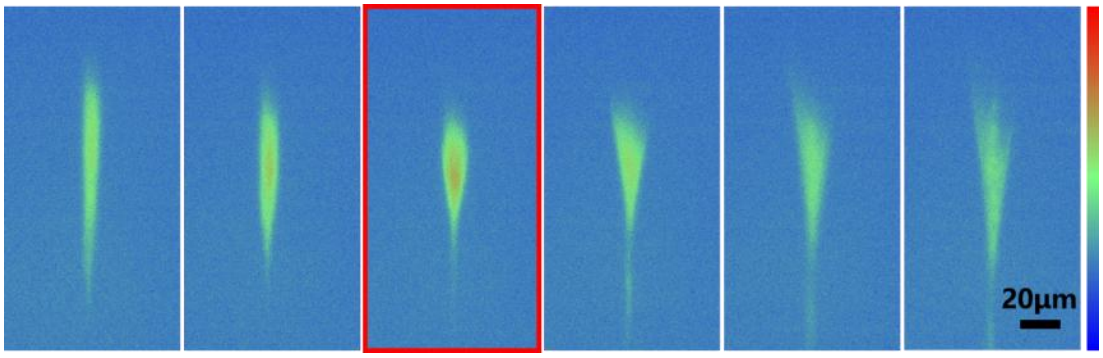

Fig. S1. Luminescence images of rotation with correction ring. The laser energy is 1μJ with single pulse. The corresponding correction ring position in the red box is the machining position.

2. Multi-line scanning with 2 and 32 sub-pulses

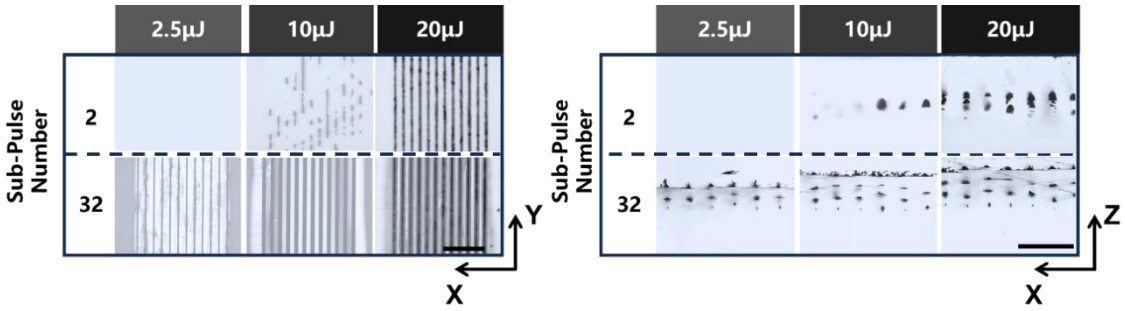

Fig. S2. Laser multi-line scanning with 2 and 32 sub-pulses. (a) Top view of modification aera and microcracks. The scale bar represents 400μm. (b) Side view of modification aera and microcracks. The scale bar represents 200μm.

3. Laser scanning speed optimization

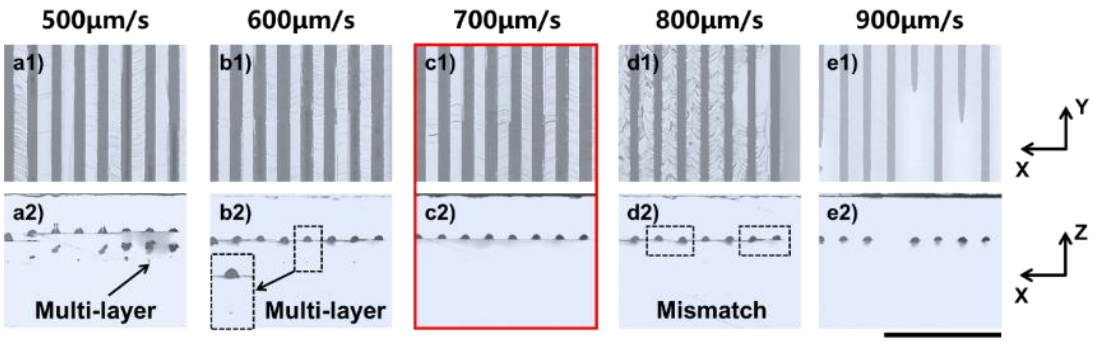

Fig. S3. Laser multi-line scanning with different scanning speed. Top view and side

view of modification aera and micro-cracks. The scale bar represents 400μm.

Figure S3 shows top and side views of modification layers at different scanning speeds. At 500μm/s, multilayer modification occurs. Increasing to 600μm/s still causes small modification points below the crack layer. At 700μm/s, single-layer modification-crack growth is achieved, avoiding multilayer modification, with smooth crack layer extension. At 800μm/s, single-layer modification-crack growth continues, with minor fluctuations in crack induction. At 900μm/s, laser modification occurs without crack extension. Thus, a scanning speed around 700μm/s achieves single-layer modification-crack growth with a thickness under 20μm.

4. Laser scanning interval optimization

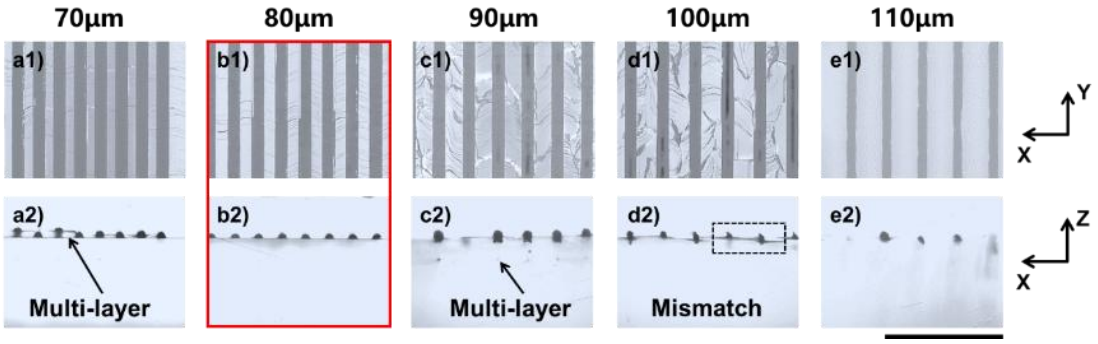

Fig. S4. Laser multi-line scanning under different scanning interval. Top view and side view of modification aera and micro-cracks. The scale bar represents 400μm.

Figure S4 shows top and side views of modification layers at different scanning intervals. At 70μm, stable modification-crack layers form but with unstable crack extension above them due to laser reflection on pre-existing microcracks. Larger intervals cause unstable crack extension and significant height fluctuations in the crack layer. Thus, appropriate scanning intervals are crucial for smooth modification-crack layer growth.

5. Comparison between our temporally shaped pulses and conventional pulse duration extension methods

To address the comparison between our temporally shaped pulses and conventional pulse duration extension methods, we conducted additional luminescence observation

experiments. The experimental results are shown in the Figure S5. Using a 1 kHz repetition rate, 1030nm laser focused inside a silicon carbide crystal with a 0.65 NA correction-collar objective (pulse energy: 400nJ), we compared two configurations: a) an 8-subpulse train with total duration matching b) a single 3.9ps pulse. Luminescence imaging revealed stronger carrier excitation using our temporal shaping approach under identical total pulse energy.

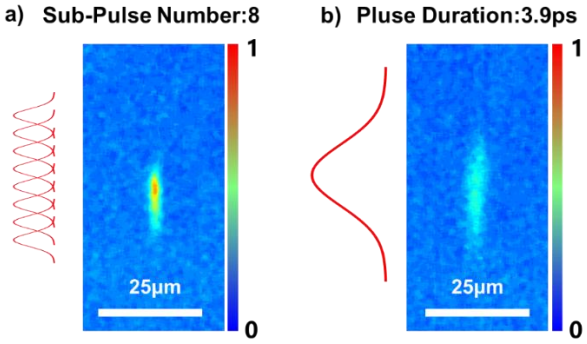

Fig. S5 a) Internal luminescence images for 8 sub-pulses train. b) Internal luminescence images for single pulse with 3.9ps pulse duration.

This enhancement originates from fundamental differences in energy deposition dynamics: While the single ps pulse's high peak energy induces premature carrier generation before reaching maximum intensity - causing subsequent energy shielding at the focal front - our sub-pulse sequence with reduced peak energies enables progressive energy accumulation. Each sub-pulse creates localized excitation within a shorter axial range, allowing subsequent sub-pulses to deposit energy precisely within this confined region. This prevents focal shift caused by excessive peak intensity while achieving more efficient excitation compared to conventional pulse broadening methods.

6. Side view of the sliced crystal

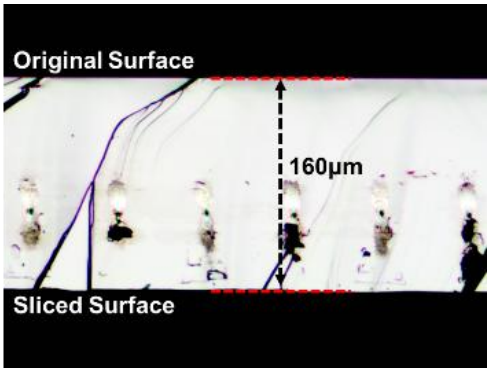

Fig. S6 Side view of the sliced crystal. The thickness is 160μm.

7. Surface morphology and characterization of sliced wafer

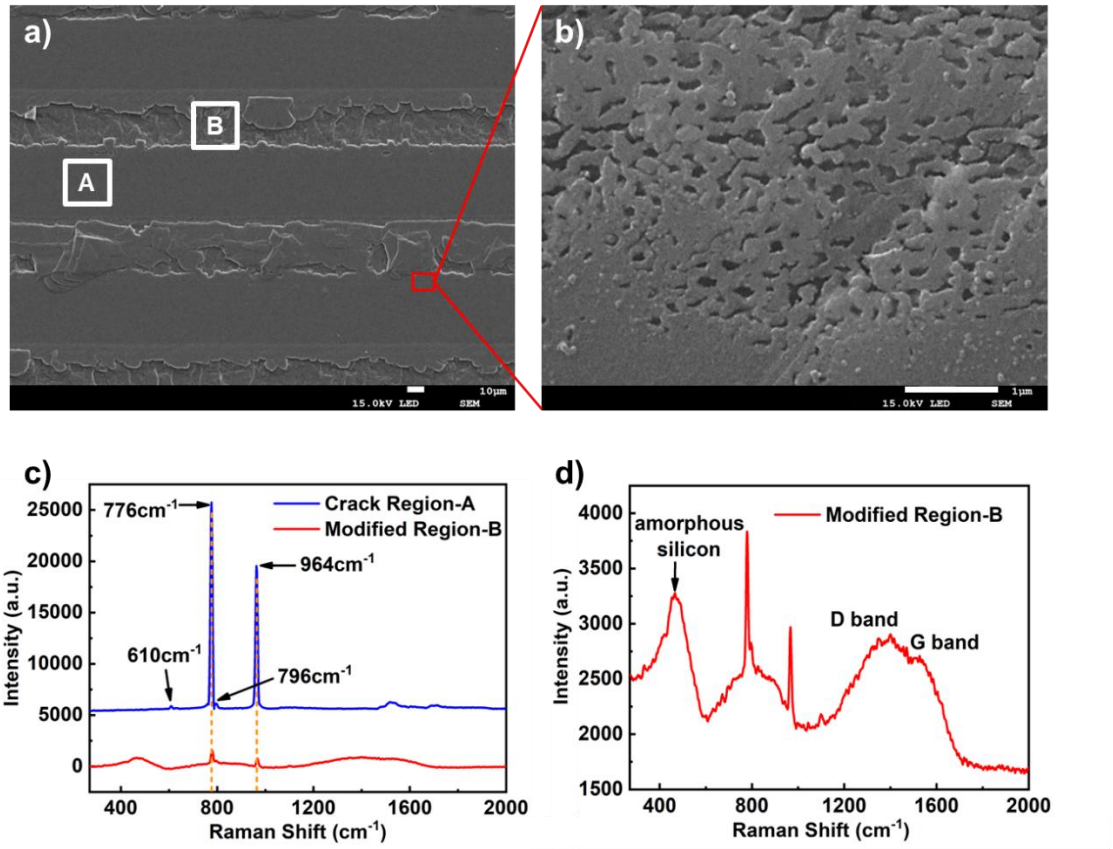

Fig. S7. Scanning electron microscopy and Raman spectroscopy characterization of sliced silicon carbide crystal surface.

Figure S7 a) displays multiple modification lines along with crack propagation areas. By magnifying the edge of a modification line, we observe micro-porous structures, as shown in Figure S7 b). These structures may have been formed by micro-explosions within the modified region.

The Raman spectra were obtained with a 532 nm laser and covered a range of 270-2000 cm^{-1}. In 4H-SiC, the fundamental folded mode branches include the transverse acoustic (FTA), longitudinal acoustic (FLA), transverse optical (FTO), and longitudinal optical (FLO) modes. Figure S6 c) shows the Raman spectra of crack extension region A and the modification region B. The Raman spectra A indicate that the chemical composition and bonding structure in this area remain largely unchanged. Characteristic peaks of 4H-SiC are present, including the LA mode at 610 cm^{-1}, TO modes at 776 and 796 cm^{-1}, and the LO mode at 964 cm^{-1}. After 1400 cm^{-1}, some weaker impurity peaks appear, likely due to surface contaminants or oxides introduced during the exfoliation process, such as the D and G bands of carbon contaminants.

Figure S7 d) shows the magnified Raman spectra of laser-modified region. In this spectrum, the characteristic peaks of the 4H-SiC crystal are significantly weakened. Additionally, a broad peak appears around 480 cm^{-1}, indicating the presence of amorphous silicon in this area. The broad peaks in the range of 1300 cm^{-1} to 1600 cm^{-1} further suggest the existence of an amorphous carbon structure. These peaks imply that structural decomposition of silicon carbide occurred during the laser modification process.

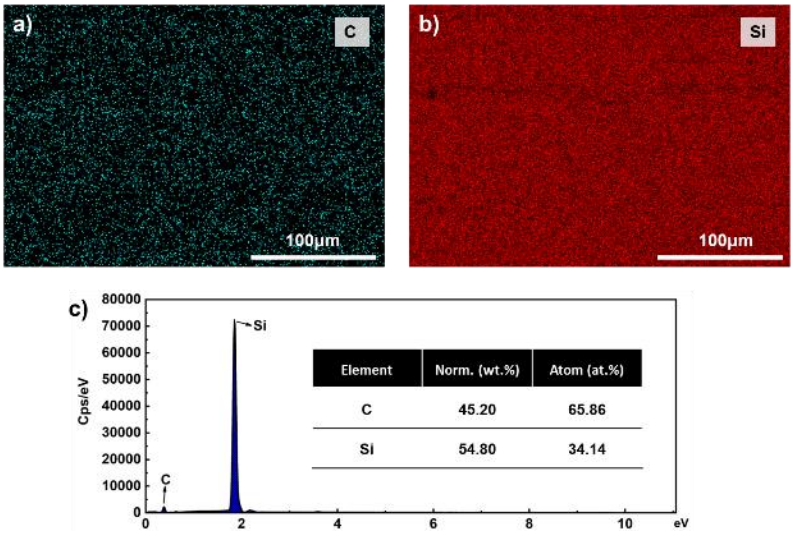

Fig. S8 EDS elemental distribution and chemical composition (wt.% and at.%) correspond to the SEM image Fig. (a).

9. Research block diagram of this paper

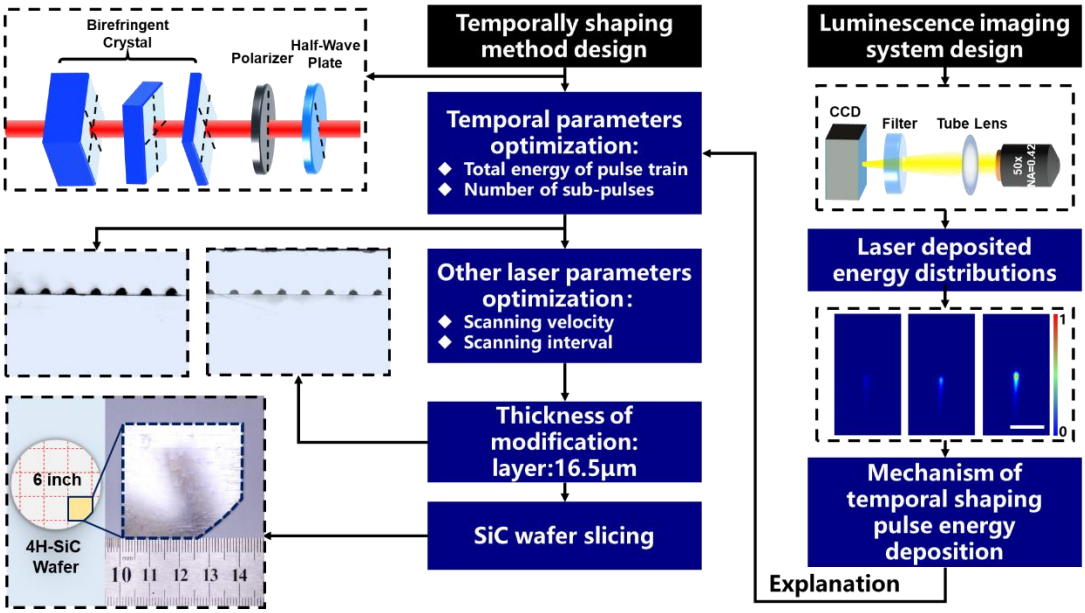

Fig. S9 The research block diagram.